InterPore JOURNAL

Please cite the following article as:

Haese, R., & Jyoti, A. (2026). Modelling copper mobilisation from low-grade ore controlled by mineral surface reactions. *InterPore Journal*. Advance online publication. https://doi.org/10.69631/q237yd92

Received: 12 Sept. 2025
Accepted: 21 Feb. 2026
Published Online (Accepted Version): 18 Mar. 2026

Modelling copper mobilisation from low-grade ore controlled by mineral surface reactions

Ralf R. Haese[1*], Apoorv Jyoti[1]

[1]School of Geography, Earth and Atmospheric Sciences, The University of Melbourne, Parkville, Victoria 3010, Australia

*** Correspondence:**
*Corresponding Author: ralf.haese@unimelb.edu.au

Keywords: Coupled dissolution and reprecipitation, copper leaching, pore scale, reactive-transport model

Abstract

Many metals of economic value are commonly recovered from low grade ores through heap leaching at mine sites. The recovery of metals in heaps is often limited for multiple reasons including mineral overgrowth of targeted minerals resulting in suboptimal mineral dissolution rates. Chalcopyrite is a major copper iron sulphide mineral found in copper sulfide ores and its dissolution is controlled by multiple dissolution reaction mechanisms and potential mineral overgrowth. Traditional continuum scale reactive-transport models including those applied to simulate heap leaching do not account for local, mineral surface-controlled processes which may have implications for large-systems such as copper recovery in heaps. A new finite element, multicomponent reactive-transport model was developed and enabled the simulation of concurrent reactions at the discrete chalcopyrite surface and its surrounding gangue mineral and the fluid phase. The model predicts the rate of chalcopyrite dissolution controlled by different reaction mechanisms (proton- and ferric-iron promoted) as well as the rate of secondary mineral formation (jarosite) at the mineral surface. The latter may increasingly inhibit copper mobilisation over time through surface passivation. The onset and growth of the surface passivation layer is largely controlled by the surrounding fluid composition and ion transport through the gangue mineral. The reduction in porosity of the surface passivation layer leads to the breakdown of ionic transport to the chalcopyrite surface and associated copper mobilisation. Maximum copper recovery is achieved by high ferric iron concentrations and low pH and by preventing the formation of a passivation layer by keeping the sulphate concentration low.

1 Introduction

As the world transitions to a low CO_2 emission economy, the demand for copper has surged to an all-time high level because copper is the most widely used metal in renewable energy technologies including batteries and electric vehicles. The global copper demand is predicted to gradually increase by up to a factor of three by 2050 (1). With the increase in copper production the quality of the copper ore also referred to as the ore grade will decline (2, 3), in other words copper recovery from low-grade ore will become increasingly important. A sufficient supply of copper is a concern for the energy transition as it is estimated that the copper demand will exceed copper resources in the second half of this century (4). These predictions point to the need to increase the proportion of recycled copper and to enhance the recovery of copper from low-grade ore.

One of the processes limiting copper recovery from low-grade ore is mineral overgrowth at the surface of the copper-containing mineral which is often the mineral chalcopyrite (5). The mineral overgrowth is also referred to as passivation or coupled dissolution and reprecipitation (CDR). The widespread and important occurrence of CDR in a large range of geological systems and their thermodynamic and kinetic constraints were presented in landmark studies by Putnis (6, 7). As explained by Ruiz-Agudo and colleagues (8), “the dissolution of a mineral by an aqueous solution results in an interfacial fluid film that may become supersaturated with respect to a new mineral phase, and that this phase may nucleate within this interfacial region. The common observation in both nature and experiment that one solid phase can be replaced by another via coupled dissolution–precipitation suggests that this is a universal mechanism of re-equilibration during fluid–mineral interaction.” A large diversity and complexity of mineral textures (grain size and shape, porosity, thickness of secondary layer) at mineral boundaries was related to the diversity of mechanisms responsible for CDR (9). While observational data from natural rocks are abundant (see review by (9)) and some experimental studies (for example

(10, 11)) have been published on CDR, numeric models simulating concurrent dissolution and reprecipitation reactions at mineral surfaces have only been developed in recent years (12 - 14).

Heap leaching is a key technology that is used to recover metals from low grade ores. A heap is a large pile of poorly sorted low-grade ore, where a reagent as referred to lixiviant constantly infiltrates and leaches targeted metals from the rocks. The metal-enriched fluid is collected at the base of the heap. A heap is spatially complex and dynamic in time in terms of the thermal, hydrodynamic and mechanical conditions and the chemical reactions. This makes the numerical modelling of such a system a challenge even though the mathematical modelling of heap leaching has been studied over the last 20 years (15-19). HEAPSIM is one of the most comprehensive heap models used extensively to simulate a variety of processes in different ores (15, 20). In case of copper recovery through heap leaching, chalcopyrite ($CuFeS_2$) is the main targeted mineral and an acid typically with a pH of 1 to 2 and highly enriched in ferric iron (Fe^{3+}) serves as lixiviant. Oxygen is injected into the heap to keep most parts oxygenated. Proton-promoted and ferric iron promoted dissolution of chalcopyrite are the principle reaction mechanisms for the mobilisation of copper (21, 22). The rate of chalcopyrite dissolution is often slow which is typically due to mineral overgrowth of the chalcopyrite surface (23, 24). Secondary minerals in the form of jarosite ($KFe_3(SO_4)_2(OH)_6$), covellite (CuS) and hematite (Fe_2O_3) are potential secondary minerals which can form at the chalcopyrite surface.

iCP is a user-friendly reactive-transport model combining COMSOL and PhreeqC (25) and was used to model the coupling of transport and reactions in copper heaps to overcome the lack of specific mineral-water reactions in previous models (26). More recently, iCP was further used for reactive-transport modelling at pore scale where, for example, reaction rates are predicted at discrete mineral boundaries (27).

Complementary to the existing models simulating coupled dissolution and precipitation at mineral surfaces and processes in heap systems at continuum scale, iCP was used in this study to develop a multi-component reactive transport model combining continuum and discrete modelling techniques in order to simulate transport and reactions at the surface of a single grain composed of chalcopyrite surrounded by gangue mineral and lixiviant. The model allows the implementation of kinetically controlled dissolution and precipitation reactions at reactive mineral surfaces. A series of simulations with variable parameters (pH, dissolved Fe^{3+} and oxygen concentrations, flow velocity, volume ratio of chalcopyrite to gangue mineral) were run to investigate CDR processes at the surface of chalcopyrite and their consequences for copper recovery.

2 Materials and Methods

2.1 Conceptual model

A 2-dimensional (2D) model was developed to simulate dissolution reactions at the surface of chalcopyrite, secondary mineral precipitation within a thin layer surrounding the chalcopyrite and a number of reactions in the gangue mineral with microporosity outside of the precipitation layer and in the free fluid. The model combines the concepts of continuum scale where averaged properties such as porosity and permeability are used and discrete modelling where phases are spatially separated for example in a pore network where pores filled with fluid are spatially separate from grains. The modelling approach is similar to the ones by Mollins and colleagues (28) and Soulaine (29 and references therein). The model development and its implementation in iCP is an extension of an earlier study by the authors (27) which modelled mineral surface reaction rates and dynamic changes to the grain shape and were validated against experimental results.

At the center of the model is a 2D circular, solid phase chalcopyrite grain ($\Gamma_{\text{chalcopyrite}}$) where no fluid or ionic transport is allowed (Fig. 1). The boundary of the solid chalcopyrite grain is explicitly defined ($\gamma_{\text{chalcopyrite}}$), and chemical reactions are allowed to take place at this boundary. The solid chalcopyrite domain is completely enclosed by a thin layer where jarosite can precipitate $\left(\Gamma_{jarosite}\right)$. Adjacent to the thin precipitation layer is a layer of gangue mineral in the form of quartz $\left(\Gamma_{\text{quartz}}\right)$. Figure 1 shows the chalcopyrite and gangue mineral grains with a diameter of 0.2 and 0.4 cm, respectively, resulting in a grain ratio of 1:2. The jarosite precipitation layer and the gangue mineral layer are treated as a porous media, where a porosity and permeability are defined and govern fluid flow and transport. The outer free fluid domain (Γ_{pores}) surrounds the gangue mineral layer. The free fluid enters from the inlet (γ_{inlet}) and exits the model from the outlet (γ_{outlet}) boundary.

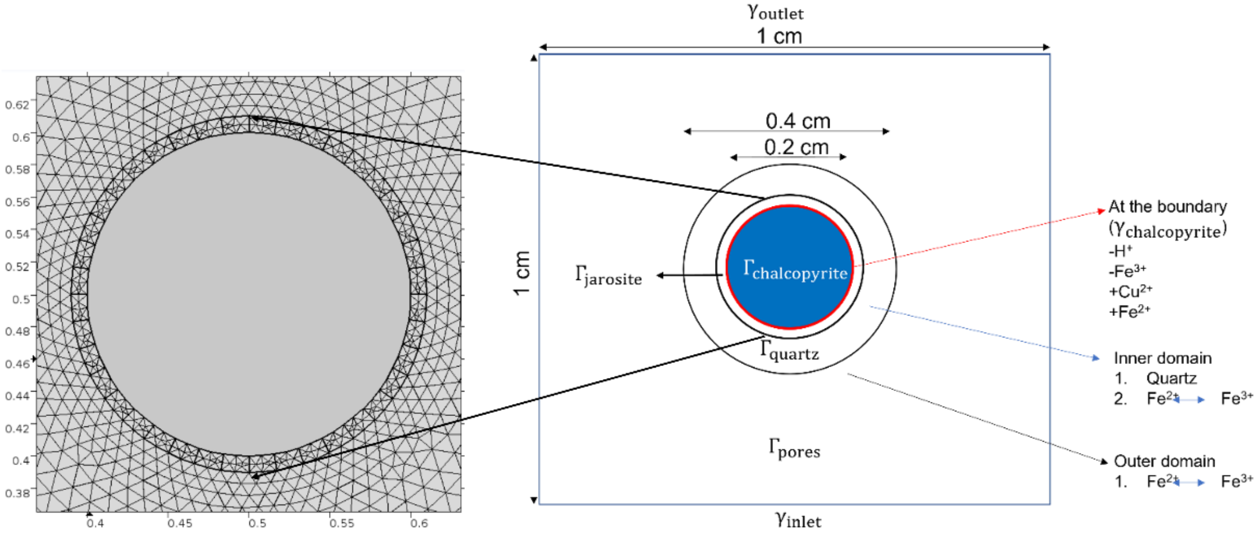

Figure 1: The model setup and the refined mesh used for the numerical model. The red circle represents the discrete reactive mineral surface.

2.2 Model set-up

The solid chalcopyrite grain $\left(\Gamma_{\text{chalcopyrite}}\right)$ has a radius of 1 mm. The thin porous layer surrounding the solid chalcopyrite grain $\left(\Gamma_{jarosite}\right)$ has a thickness of 0.1 mm and consists of 480 grid cells of equal size. In case of a chalcopyrite to gangue mineral grain ratio of 1:2 (Fig. 1), the thickness of the porous gangue mineral layer $\left(\Gamma_{\text{quartz}}\right)$ is 1 mm and the quartz surface area is 22.64 m^2 Kg^{-1} (see SI Eq 10). The gangue mineral layer consists of 1654 grid cells, which increase exponentially in size from the inside out. For the porous media ($\Gamma_{jarosite}$, Γ_{quartz}) the permeability was defined as $1e^{-13}\ m^2$ and the porosity as 0.1.

A fluid flow equation is used which connects the free flow domain to the porous media. To achieve this the Brinkman equation for the porous media part and the Navier Stokes equation for the free flow part is used (17). The same fields, velocity $\boldsymbol{u}$ (m s^{-1}) and pressure p (Pa) were solved in the free flow domain (Γ_{pores}) and the porous domain ($\Gamma_{\text{quartz}} + \Gamma_{jarosite}$). This enforces a continuity between the fluid velocity in the free flow and the Darcy velocity in the porous domain. Details of the Navier-Stokes equation and the Brinkman equation are given in SI Section 1.

Once the velocity and the pressure fields for the free and porous media domains are resolved, the transport and reaction of species can be solved using the standard advection-diffusion-reaction equation for each of the components in the aqueous phase (30). Details of the advection-diffusion-reaction equation are given in SI Section 2.

The boundary conditions for the inlet and outlet boundaries were defined as follows with the left and the right boundary (Fig. 1) assigned no-flow: The inflow velocity was set to $1.25\mathrm{e}^{-6}$ m s^{-1} and the outlet pressure to 101325 Pa.

For the jarosite domain, $\Gamma_{jarosite}$, the change in porosity due to the precipitation of jarosite alters the diffusive flux, which is calculated as (31):

$$\frac{\partial c_i}{\partial t} = -\emptyset'_{\Gamma_{jarosite}} \nabla \cdot \left(\nabla D_{eff} c_i\right)\Big|_{\Gamma_{Jarosite}} \tag{1}$$

With $\emptyset'_{\Gamma_{jarosite}}$ being the porosity in the jarosite domain, D_{eff} is the effective diffusion coefficient and ∇ci is the concentration gradient.

The effective diffusion coefficient is calculated as $D_{eff} = \frac{D_{Diff}}{\theta^2}$, where D_{Diff} is the diffusion coefficient in water ($1e^{-9}\ m^2\ s^{-1}$) and tortuosity, θ, is calculated as $\theta = 1 - \ln\left(\emptyset'_{\Gamma_{\text{jarosite}}}\right)^2$.

For calculating the dynamic changes in porosity in the jarosite domain ($\emptyset'_{\Gamma_{jarosite}}$), the moles of jarosite precipitated ($mole_{jaro}$) is calculated for each time step. The volume of the precipitated jarosite (Vol_{jaro}) is calculated as:

$$Vol_{jaro} = \frac{M_{jaro}}{\rho_{Jaro}} \tag{2}$$

Here ρ_{Jaro} = 3.9 (g cm^{-3}), M_{jaro} is the mass of jarosite and is calculated as:

$$M_{jaro} = W_{jaro} * \ mole_{jaro} \tag{3}$$

Here, molecular weight of jarosite W_{jaro}= 500.8 (g mol^{-1}) and $mole_{jaro}$ is the amount of jarosite moles precipitating calculated from the model.

Next, the new porosity $\emptyset'_{\Gamma_{jarosite}}$ is calculated as:

$$\emptyset'_{\Gamma_{jarosite}} = \frac{(Vol_{\Gamma_{jarosite}} - Vol_{mineral})}{Vol_{\Gamma_{jarosite}}} \tag{4}$$

Here $Vol_{\Gamma_{jarosite}}$ is the volume of the jarosite domain, $Vol_{mineral}$ is the total volume of the solid phase in the jarosite domain which is calculated as:

$$Vol_{mineral} = Vol_{\Gamma_{jarosite}} * \left(1 - \emptyset'_{\Gamma_{jarosite}}\right) + Vol_{jaro} \tag{5}$$

The calculated new porosity ($\emptyset'_{\Gamma_{jarosite}}$) from Eq. 4 is used in the diffusive flux equation (Eq. 1) to calculate the change in concentrations of the aqueous species due to the altered porosity at each time step. Note, chemical reactions are here written and referred to as equations.

Two reaction mechanisms lead to the dissolution of chalcopyrite at its surface, ($\gamma_{\text{chalcopyrite}}$), (21):

1) The proton-promoted reaction:

$$\mathrm{CuFeS_{2(s)} + 4H^{+}_{(aq)} = Cu^{2+}_{(aq)} + Fe^{2+}_{(aq)} + 2H_2S} \tag{6}$$

2) The Fe^{3+}- promoted dissolution:

$$\mathrm{CuFeS_{2(s)} + 16Fe^{3+}_{(aq)} + 8H_2O_{(aq)} = Cu^{2+}_{(aq)} + 17Fe^{2+}_{(aq)} + 16H^{+}_{(aq)} + 2SO^{-2}_{4(aq)}} \tag{7}$$

Rates of the two reactions are calculated as a function of the proton (H^{+}) and Fe^{3+} activities; details of the rate equations are given in SI Section 3.

Reactions at the mineral surface can be explicitly defined without the need to define the mineral reactive surface area as an input to the model (27). Instead, the mineral surface area is calculated by integrating the local surface area of each boundary cell over the actual reactive boundary. The rate is integrated on the reactive boundary ($\gamma_{\text{chalcopyrite}}$) and a molar flux of the aqueous phase, $J_i = \int_{S_{\text{chalcopyrite}}} \acute{R}_a . dS$ ($\mathrm{mol\,s^{-1}}$), is computed for each species i, $\acute{R}_a$ is the reactions rate of the chalcopyrite using SI Eq. 7 and SI Eq. 8 given in SI section 3, $S_{\text{chalcopyrite}}$ is the surface area of the mineral grain which is directly calculated from the model. This flux controls the molar mass of the species in or out of the aqueous phase due to surface reactions and is calculated in COMSOL. A constant equilibrium phase of atmospheric oxygen pressure is imposed on the system except for simulations 11 and 12 (Table 1).

There are kinetically-controlled reactions taking place in the two porous media domains, the chalcopyrite precipitation domain, $\Gamma_{\text{chalcopyrite}}$, and the quartz domain, Γ_{quartz}, (Fig. 1). The dissolution of quartz, $SiO_2(s) + 2H_2O = H_4SiO_4$, within the quartz domain is calculated as a function of the state of saturation according (32). Details of the rate equation for quartz dissolution are given in SI Section 3.

The precipitation of jarosite within the jarosite precipitation domain, $\Gamma_{\text{chalcopyrite}}$, is defined as

$$KFe_3(SO_4)_2(OH)_6 + 6H^+ = 3Fe^{3+} + 6H_2O + K^+ + 2SO_4^{2-} \tag{8}$$

and is thermodynamically controlled with a $\log k = -9.21$. The mass of precipitated jarosite (M_{jaro}) (Eq. 3) is calculated at each time step in PhreeqC and transferred to COMSOL for determining its effect on the porosity.

The following two oxidation reactions are implemented in the free fluid domain, Γ_{pores}:

The oxidation of ferrous iron (Fe^{2+}) with oxygen (O_2) is defined as:

$$4\mathrm{Fe}^{2+}_{(\mathrm{aq})} + \mathrm{O}_{2(\mathrm{aq})} + 4\mathrm{H}^{+}_{(\mathrm{aq})} = 4\mathrm{Fe}^{3+}_{(\mathrm{aq})} + 2\mathrm{H_2O} \tag{9}$$

The rate of the reaction is a function of the pH and the O_2 and Fe^{2+} concentrations according to (33) and is detailed in SI Section 3.

The oxidation of sulphide (H_2S) with O_2 is defined as:

$$H_2S + 2O_2 = SO_4^{2-} + 2H^+ \tag{10}$$

And the respective rate equation is given in SI Section 3.

All of the reaction rates are calculated for each time step and used in the standard advection-diffusion-reaction equation (SI Eq. 5).

In order to account for all aqueous species in solution, primary aqueous species were defined and their relationship with other aqueous species in the solution was calculated by their equilibrium constants, $K_{eq.}$ The model uses the PhreeqC database phreeqc.dat which comprises all log K_{eq} data to calculate the aqueous speciation (see also SI Section 3, SI Table 2).

The above-described model conditions were implemented as a pore-scale model with a discrete reactive mineral surface in iCP (27).

2.3 Set of simulations and their aims

A set of simulations with variable input parameters were run in this study to better understand the importance of variable processes and conditions controlling CDR and copper recovery. Table 1 lists the simulation number and the parameters used. Simulations 1-6 study the effect of pH and Fe^{3+} by varying their concentrations. Simulations 7 and 8 study the effect of SO_4^{2-} concentration on copper recovery by tracking the porosity change and the volume of secondary mineral overgrowth. Simulations 9 and 10 study the effect of gangue mineral thickness surrounding the chalcopyrite grain, simulations 11 and 12 study the effects of oxygen concentrations and simulations 13 and 14 study the effects of changing inlet velocities on the copper recovery.

Table 1. Description of the models and the parameters used. Potassium (K^+) had a concentration of 0.01 M in all simulations. The chosen fluid flow velocities are based on previous studies (34 - 36).

Aim: Dominant reaction at the chalcopyrite boundary						
Simulation No.	pH	Fe^{3+}	SO_4^{2-}	O_2	Grain Ratio	Velocity
1	1	0.01M	1×10^{-13} M	saturated	1:2	1e-6 m/s
2	1	0.005M	1×10^{-13} M	saturated	1:2	1e-6 m/s
3	1	0.001M	1×10^{-13} M	saturated	1:2	1e-6 m/s
4	2	0.01M	1×10^{-13} M	saturated	1:2	1e-6 m/s
5	2	0.005M	1×10^{-13} M	saturated	1:2	1e-6 m/s
6	2	0.001M	1×10^{-13} M	saturated	1:2	1e-6 m/s
Aim: Rate of jarosite precipitation, dynamic growth in the passivation layer and its effect on Cu^{2+} recovery						
	pH	Fe^{3+}	SO_4^{2-}	O_2	Grain Ratio	Velocity
7	2	0.01M	5×10^{-5} M	saturated	1:2	1e-6 m/s
8	2	0.01M	9×10^{-5} M	saturated	1:2	1e-6 m/s
Aim: Grain Ratio (≈ surface area of gangue mineral) and its effect on Cu^{2+} recovery						
	pH	Fe^{3+}	SO_4^{2-}	O_2	Grain Ratio	Velocity
9	2	0.01M	1×10^{-13} M	saturated	1:3	1e-6 m/s
10	2	0.01M	1×10^{-13} M	saturated	1:4	1e-6 m/s
Aim: Effect of O_2 on Cu^{2+} recovery and rate of jarosite precipitation						
	pH	Fe^{3+}	SO_4^{2-}	O_2	Grain Ratio	Velocity
11	2	0.01M	1×10^{-13} M	Half-sat.	1:2	1e-6 m/s
12	2	0.01M	1×10^{-13} M	Zero sat.	1:2	1e-6 m/s
Aim: Effect of changing velocities on the outlet Cu^{2+} concentration						
	pH	Fe^{3+}	SO_4^{2-}	O_2	Grain Ratio	Velocity
13	2	0.01M	1×10^{-13} M	saturated	1:2	1e-5 m/s
14	2	0.01M	1×10^{-13} M	saturated	1:2	1e-4 m/s

3 Results

3.1 Simulations 1 – 6

Simulations 1 to 6 were run to investigate the importance of proton-promoted as opposed to ferric iron-promoted chalcopyrite dissolution and respective copper recovery. The sulphate concentration was kept low, the O_2 concentration was continuously high (saturated) and the grain radius ratio between the chalcopyrite grain and the gangue mineral of was chosen to be 1:2 (Table 1). The change in outflow concentrations and reactions rate over time follows the trend of a breakthrough curve, where initial values are zero followed by a rapid increase before constant values are reached. The short period of rapid increase in values occurs approximately when the system is flushed the first time and marks the breakthrough time or flushing time. In the study the flushing time is about 10,000 seconds (2.8 hours) based on tracer simulations (data not shown). The last phase of the breakthrough curve shows constant values representing steady-state conditions in terms of chemical reaction rates and respective fluid composition at the outflow.

Reaction mechanism specific, steady state chalcopyrite dissolution rates vary over two orders of magnitude with the lowest rates by the ferric-promoted dissolution mechanism at pH 2 (~$1.4*10^{-16}$ mol cm^{-2} sec^{-1}, simulation 6) and the highest by the proton-promoted dissolution rate at a pH of 1 and the highest Fe^{3+} concentration ($1.25*10^{-13}$ mol cm^{-2} sec^{-1}, simulation 1) (Figure 2). Proton-promoted dissolution rates are not affected by variable Fe^{3+} concentrations whereas the ferric iron-promoted dissolution rates are increased at higher proton concentrations (simulations 1 to 3) relative to lower proton concentrations (simulations 4 to 6). The copper (Cu^{2+}) outflow concentrations reflect the chalcopyrite dissolution rates with the highest Cu^{2+} concentrations at a pH of 1 (simulations 1 to 3) and Cu^{2+} concentrations about one order of magnitude lower at a pH of 2 (simulations 4 to 6).

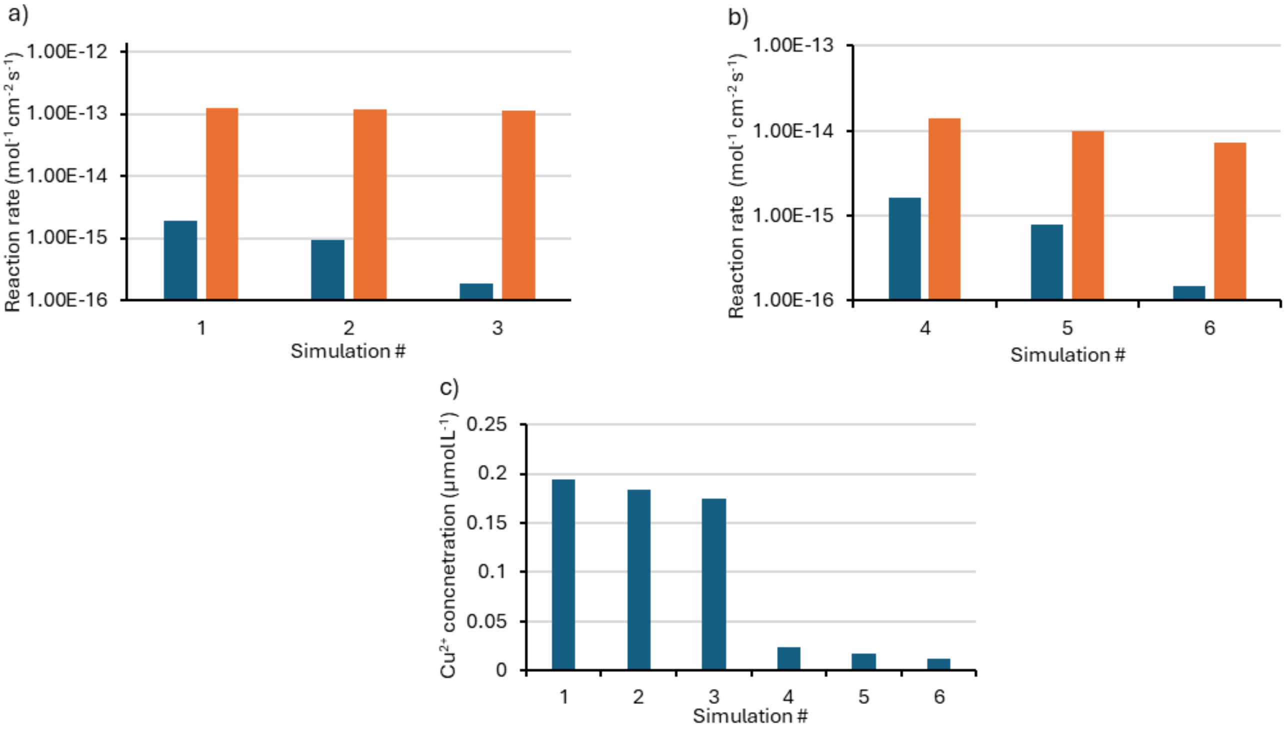

Figure 2: Steady-state chalcopyrite dissolution rates and copper outflow concentrations in simulations 1 to 6. Fe^{3+} concentrations in the inflow were 0.01 (simulations 1 and 4), 0.05 (simulations 2 and 5) and 0.1 mol/L (simulations 3 and 6). Simulations 1 to 3 had a pH of 1 (a) and simulations 4 to 6 had a pH of 2 at the inflow (b). Dissolution rates controlled by proton-promoted dissolution in orange and dissolution rates controlled by ferric iron-promoted dissolution in blue. c) Cu^{2+} concentrations at the outflow.

3.2 Simulations 7 and 8

Simulation 7 was used for the following investigations:

1. The dominant transport regime (advection vs. diffusion) was determined along a transect through the centre of the grain in order to reveal differences in transport between the free flow and the porous domains (Fig. 3a). The Péclet number (Pe′) was calculated, $Pe' = u_{in} * w * D_{diff}^{-1}$, with u_{in} is the inflow velocity, w is the domain width (0.01m) and D_{diff} is the diffusion coefficient (10^{-9} m^2 s^{-1}). A $Pe' > 1$ and a $Pe' < 1$ indicate advection and diffusion dominated regimes, respectively. As can be

seen in Figure 3b, the free flow domain is advection dominated, while the porous domain is diffusion dominated.

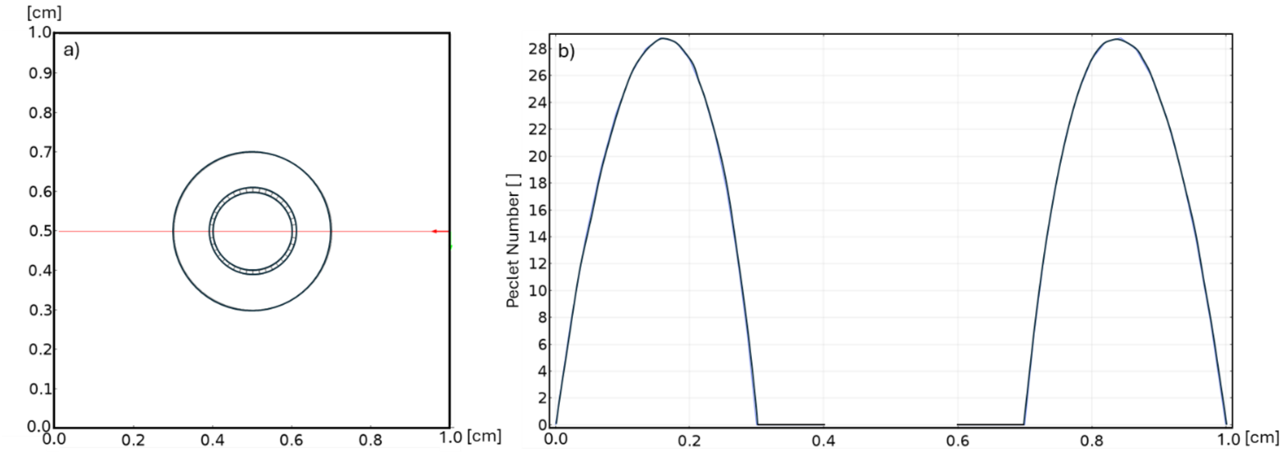

Figure 3: Advection vs. diffusion dominated transport along a horizontal transect through the centre of the grain (a). Pe′ > 1 in the free flow zone (0 – 0.3 and 0.7 – 1.0 cm along transect) indicate transport is advection dominated, while Pe′ < 1 in the porous zone (0.3 – 0.4 and 0.6 – 0.7 cm along the transect) indicate a diffusion dominated transport regime (b).

2. The spatial-temporal evolution of the Cu^{2+} concentration distribution was followed from the beginning of the simulation (0 sec) until 20,000 sec (≈ 5.5 h). The Cu^{2+} inflow concentration is ‘0’ at all times, but the Cu^{2+} concentration increases to over $7 * 10^{-7}$ M within the jarosite domain adjacent to the chalcopyrite surface (Fig. 4). A steep Cu^{2+} concentration gradient occurs from the mineral surface to the outer boundary of the porous domain. Given the porous domain is diffusion dominated, see above, the Cu^{2+} flux to the free flow domain is diffusion controlled. In contrast, once the Cu^{2+} reaches the free flow domain, its transport is advection dominated as illustrated by the pear-shaped Cu^{2+} plume.

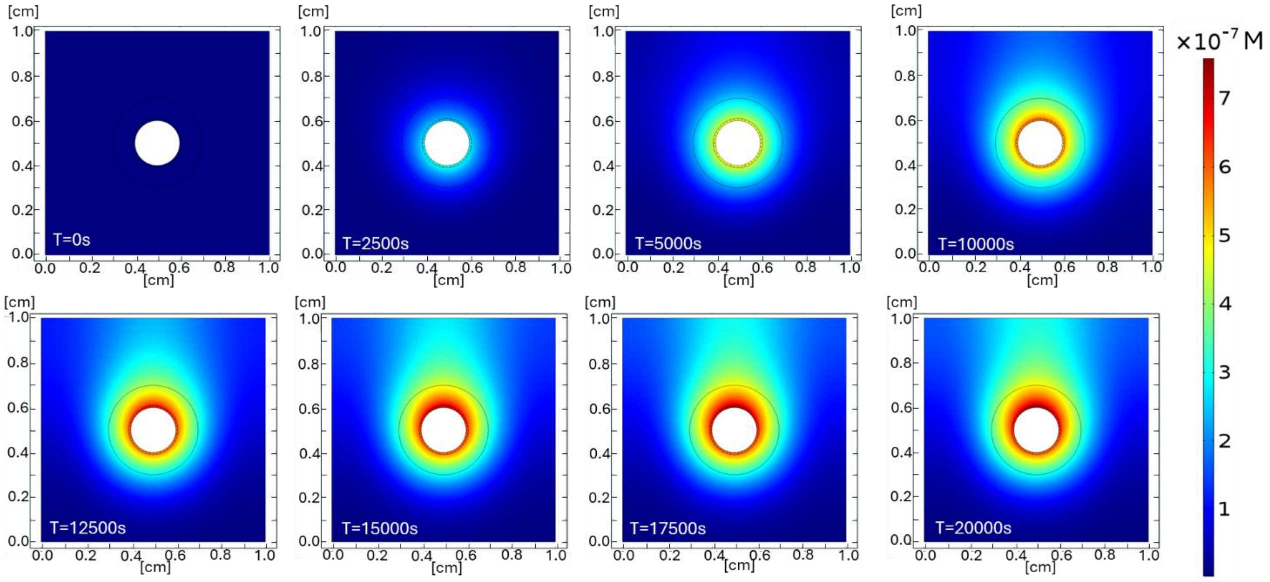

Figure 4: Spatial-temporal evolution of Cu^{2+} concentration [M] during the first 20,000 seconds (≈ 5.5 h) of Simulation 7. Note, the Cu^{2+} inflow concentration is ‘0’ at all times (at the bottom of the domain) and the chalcopyrite surface is the source of dissolved Cu^{2+}.

3. Concentration distributions for Cu^{2+}, Fe^{3+} and H^+ are shown to reveal concentration gradients controlled by the coupled dissolution and reprecipitation (Fig. 5). As shown above (Fig. 4), the chalcopyrite surface is the source of dissolved Cu^{2+} and the porous domain is characterised by a distinct concentration gradient from the mineral surface to the outer bound (Fig. 5a). Together with a $Pe' < 1$ in the porous domain, see above, Cu^{2+} transport through the porous domain to the free flow domain is diffusion controlled. The pattern of the H^+ concentration distribution (Fig. 5b) is very similar to Cu^{2+} distribution (Fig. 5a) suggesting the chalcopyrite surface is a source of H^+. This can be reconciled through the balance of reactions occurring in the jarosite domain adjacent to the chalcopyrite surface: Ferric iron – promoted chalcopyrite dissolution (Eq. 7) and jarosite precipitation (Eq. 8) produce H^+ while proton-promote chalcopyrite dissolution (Eq. 6) consumes H^+. Here, the H^+ production outcompetes the H^+ consumption. The Fe^{3+} inflow concentration is 0.01 M (Tab. 1) and its concentration drops to a minimum of about 0.001M in the jarosite domain (Fig. 5c) due to the precipitation of jarosite (Eq. 8) and the ferric iron reduction during the ferric iron – promoted chalcopyrite dissolution (Eq. 7). The rate of ferrous iron oxidation by oxygen (Eq. 9) is apparently too slow to compensate for the rate of ferric iron consumption.

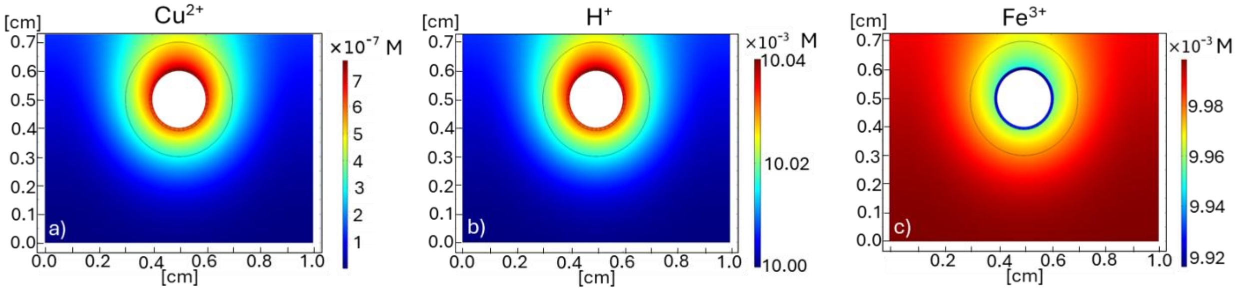

Figure 5: Spatial distribution of Cu^{2+} (a), H^+ (b) and Fe^{3+} (c) concentrations after 20,000 s of Simulation 7. Note, Cu^{2+} and H^+ are produced at the chalcopyrite surface while Fe^{3+} is consumed. The inflow is at the bottom of the domain.

Simulations 7 and 8 investigate the effects of variable sulphate concentrations on the potential formation of the passivation layer and the associated decline in the chalcopyrite dissolution rate and copper mobilisation. The Fe^{3+} concentration (0.01 mol/L) and the pH (pH of) were kept the same in both simulations, but the sulphate concentration was varied between $5 * 10^{-5}$ (simulation 7) and $9 * 10^{-5}$ (simulation 8) mol/L. The simulations were run for about 14 hours (50,000 s).   from a very small value to 0.49 and 1.003 for sulphate inflow concentrations of $5*10^{-5}$ (simulation 7) and $9*10^{-5}$ (simulation 8) mol/L, respectively. Even though the pH (= 2) and the Fe^{3+} inflow concentration (0.01 M) were the same in simulations 4, 7 and 8, the maximum copper mobilisation and outflow concentration is only about half in simulations 7 and 8 ($1.18*10^{-8}$ mol/L) compared to the maximum (steady state) concentration in simulation 4 ($2.33*10^{-8}$ mol/L) (Fig.). The onset of jarosite precipitation and the associated reduction in porosity (Figure , c) occurs while jarosite is still undersaturated (Fig.). The Cu^{2+} outflow concentration starts to decline when the porosity in the jarosite precipitation domain decreased from 0.1 to about 0.05 (Fig.). Figure shows the change in porosity along a transect across the jarosite precipitation domain. The initial porosity in the whole domain was 0.1, which changed to a porosity gradient across the domain and with time.

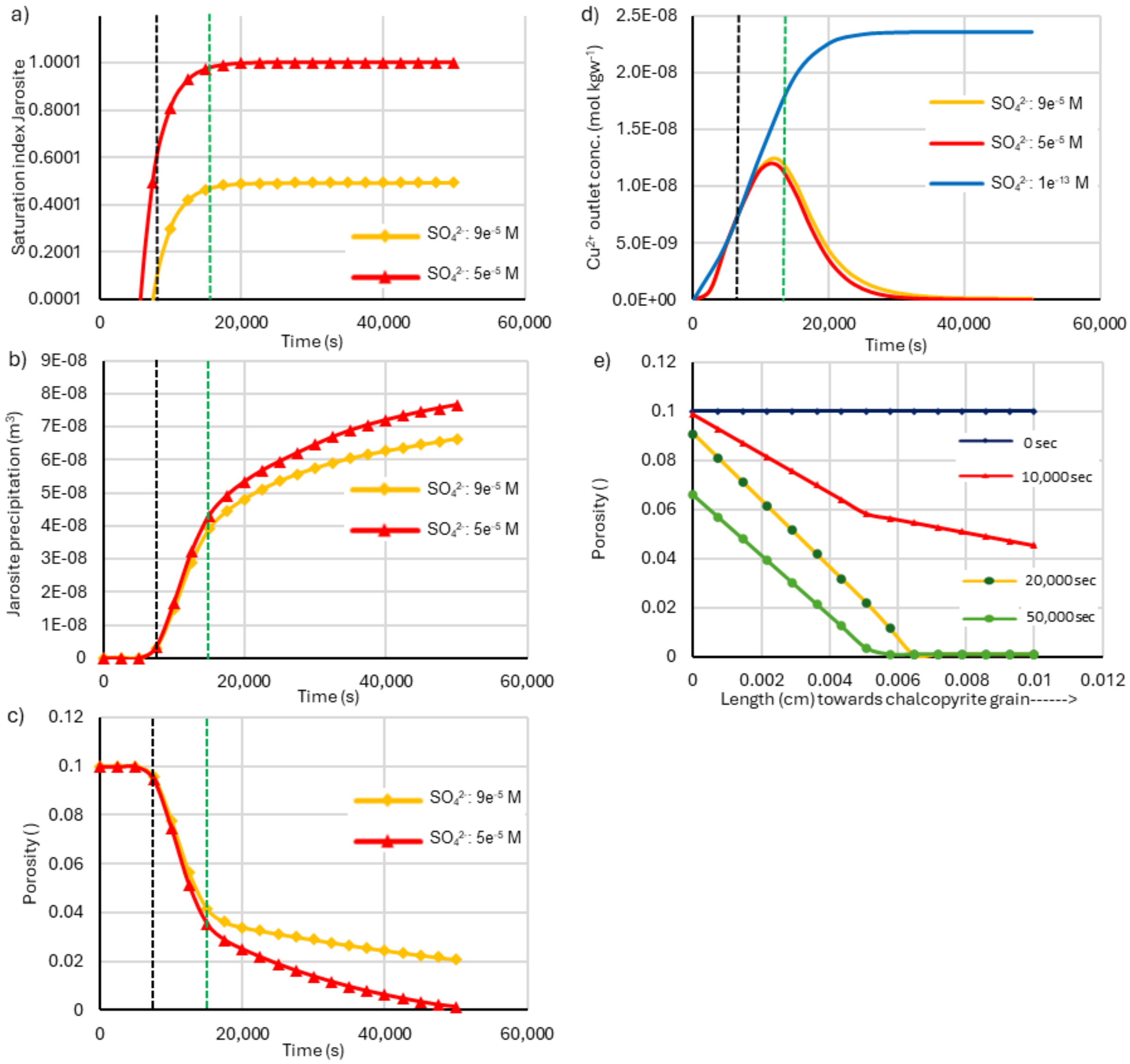

Figure 6: a) Jarosite saturation within the jarosite precipitation domain with two sulphate inflow concentrations (simulation 7 and 8). b) Change in jarosite volume within the jarosite precipitation domain. c) Change in porosity within the jarosite precipitation domain. d) Change in copper outflow concentrations without jarosite precipitation (blue, simulation 4) and with jarosite precipitation and with two different SO_4^{2-} concentrations (simulations 7 and 8). e) Change in porosity along a transect across the jarosite precipitation domain with a thickness of 0.01 cm. The black stippled line signifies the commencement of jarosite precipitation. The green stippled line signifies the time when a steady state in the saturation index for jarosite is reached at the outflow.

3.3 Simulations 9 to 12

Simulations 9 and 10 investigated the potential influence of variable gangue mineral (quartz) to chalcopyrite ratio. An injection fluid with pH 2 and a 0.01 M Fe^{3+} is used and the ratio of the chalcopyrite to quartz mineral was varied between 1:2 (simulation 4), 1:3 (simulation 9) and 1:4 (simulation 10). Steady state Cu^{2+} outflow concentrations varied for different ratios. A Cu^{2+} outflow concentration of $1.8*10^{-7}$ mol/L for a ratio of 1:2, a concentration of $1.9 * 10^{-7}$ mol/L for a ratio of 1:3

and a concentration of $2.2 * 10^{-7}$ for a ratio of 1:4 were observed. These are very small variations in the copper outflow concentration compared to the range of outflow concentrations observed in simulations 1 to 6, which changed by more than an order of magnitude (Figure 1).

Simulations 11 and 12 investigated the potential influence of variable oxygen concentrations in the inflow. All variables remained the same, but the oxygen concentration varied from fully saturated (simulation 4) to half-saturated (simulation 11) and oxygen-depleted (simulation 12). No variations in the Cu^{2+} outflow concentrations were observed, which can be explained by the very slow rate of ferrous iron oxidation using oxygen at a low pH (see also section 4.3).

3.4 Simulations 13 and14

Simulations 13 and 14 investigated the effects of fluid inflow velocities on chalcopyrite dissolution rates and Cu^{2+} outflow concentrations as the injection velocities are changed. All variables remained the same as in simulation 4 except for the injection rate. The ferric-promoted dissolution rate changed from $1.62*10^{-15}$ at a flow velocity of 1e-6 m/s to a maximum rate of $2.4*10^{-11}$ mol cm^{-2} s^{-1} at a flow velocity of 1e-4 m/s. The proton-promoted rate also increased from $1.39*10^{-14}$ to $2.06*10^{-10}$ mol cm^{-2} s^{-1} (Fig. 7a). In contrast, the Cu^{2+} outflow concentration decreased with increasing fluid inflow velocity from 0.0235 to 0.000395 µmol/L (Fig. 7b) as the mobilized dissolved copper gets increasingly diluted by the fluid not reacting with the chalcopyrite.

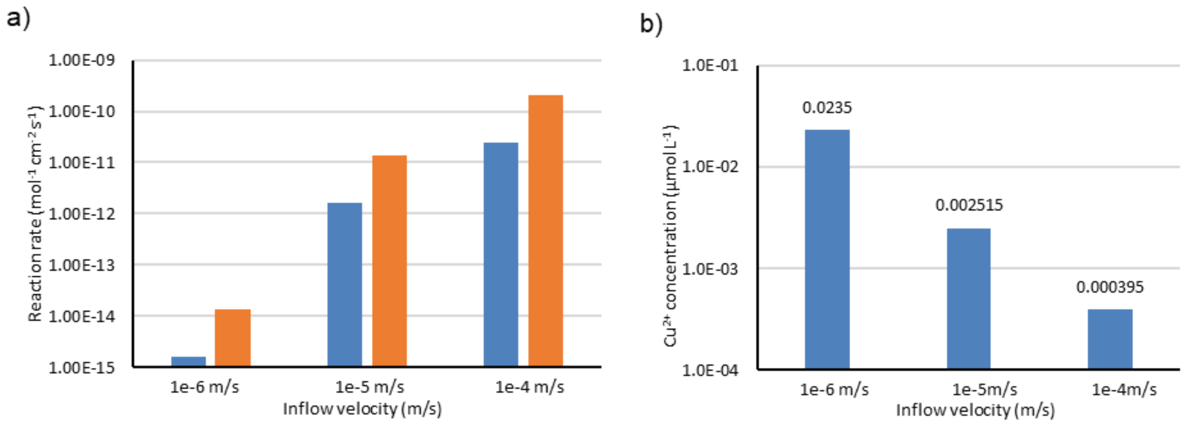

Figure 7: a) Steady-state chalcopyrite dissolution rates. Dissolution rates controlled by proton-promoted dissolution are given in orange and dissolution rates controlled by ferric iron-promoted dissolution in blue. b) Steady-state outlet Cu^{2+} concentrations at different inflow velocities.

4 Discussion

4.1 Temporal evolution of the geochemical system

It is important to recognize the temporal evolution of reaction rates and concentrations as well as changes in porosity and permeability within the jarosite domain as precipitation proceeds. At a flow rate of $1 * 10^{-6}$ m s^{-1} and a domain length of 1 cm, the fluid residence time between inflow and outflow in the free-flow domain is 10,000 s. However, ion transport through the porous domain is more variable as it is controlled by diffusion and the diffusive flux is a function of the concentration gradient and porosity (Eq. 1). Given reactions at the chalcopyrite surface produce or consume ions including H^+, Fe^{3+}, SO_4^{2-} and Cu^{2+}, the rate of these concurrent reactions affect the concentration gradients and the respective fluxes. Furthermore, the precipitation of jarosite in the jarosite domain changes its porosity, which also affects the diffusion rate. The temporal evolution of the Cu^{2+} concentration distribution (Fig. 4) illustrates the gradual changes in the Cu^{2+} concentration gradients in the porous domain and in the free-flow domain during the first 20,000 s (≈ 5.5 h). Similarly, it was demonstrated that jarosite precipitation and associated porosity reduction in the jarosite domain proceeded over 50,000 s at given conditions (Fig. 6d). From the above it is clear that CDR at mineral surfaces is a dynamic and complex interplay of ionic transport and a set of concurrent reactions.

4.2 Ion transport in the free-flow domain surrounding the grain and within the porous domain adjacent to chalcopyrite

The dominant transport mechanism is either advection or diffusion and can be calculated using the Pe′ Number (see Section 3.2). For almost all of the simulations we chose a fluid inflow velocity of $1 * 10^{-6}$ m s^{-1}, which is within the range of previously published flow velocities in heaps (Table 1). It was further assumed that the chalcopyrite grain diameter is half of the full grain diameter and the chalcopyrite grain is surrounded by gangue mineral with a low porosity (0.1) and low permeability ($1 * 10^{-13}$ m^2). In this case, it was determined that the free-flow domain is advection-dominated while the porous domain was diffusion-dominated (Section 3.2). The importance of diffusion-dominated transport adjacent to the chalcopyrite has consequences for the question whether chalcopyrite dissolution and associated Cu^{2+} mobilization is limited by the (diffusive) transport or by the reaction rate (Section 4.4)

4.3 Variability in the chalcopyrite dissolution rate in the absence of jarosite formation

Chalcopyrite dissolution rates varied over two orders of magnitude within the range of conditions covered in this study (pH between 1 and 2; $Fe^{3+}_{(aq)}$ between 0.01 and 0.001 mol/L). The proton - promoted dissolution rate always outcompeted the ferric iron-promoted dissolution rate (simulations 1 to 6, Fig. 1) leading to the highest dissolution rate at a pH of 1 and a $Fe^{3+}_{(aq)}$ concentration of 0.01 mol/L. The proton-promoted dissolution rate was solely dependent on the proton concentration (pH), while the ferric iron-promoted dissolution rate was dependant on the proton and the $Fe^{3+}_{(aq)}$ concentration. This observation can be explained with the rate laws for the two reactions where the proton and $Fe^{3+}_{(aq)}$ concentrations are variables for the ferric iron-promoted dissolution reaction (SI Eq. 7) and only the proton concentration is an input to the proton-promoted reaction (SI Eq. 8).

The results of simulations with variable O_2 concentrations (simulations 12 to 14) showed no influence of O_2 on the dissolution rate suggesting a secondary reaction of $Fe^{2+}_{(aq)}$ oxidation with O_2 is negligible. This can be attributed to two reasons. Firstly, Fe^{2+} oxidation is limited to the free fluid domain. Secondly, the OH^- concentration at a pH of 2 is very low having an inhibiting influence on the oxidation rate (SI Eq. 11).

The role of the fluid advection rate around the grain composed of chalcopyrite and the gangue (quartz) mineral on the rate of chalcopyrite dissolution was explored by varying the fluid flow rate over two orders of magnitude ($1.2*10^{-6}$ to $1.2*10^{-4}$ m sec^{-1}, simulations 4, 13 and 14). The results showed chalcopyrite dissolution rates increased over four orders of magnitudes for both reaction mechanisms with the increase in flow velocity over two orders (Fig. 7a). In contrast, the $Cu^{2+}_{(aq)}$ outflow concentrations were negatively correlated with the fluid advection rate (Fig. 7b). The diffusive Damköhler number ($Da_{II} = k_a * \gamma_a * S * R^2 * \mathrm{D_{Diff}}^{-1}$) was calculated. Here k_a is the rate constant, γ_a is the activity coefficient, S is the specific grain surface area, R is the grain radius, D_{Diff} is the diffusion coefficient. For the proton-promoted dissolution reaction, the $Da_{II}^{H^+}$ is calculated as 600 and for the ferric-iron promoted reaction $Da_{II}^{Fe^{3+}}$ >>1000. This suggests that the reaction rate is much greater than the diffusion rate and the system is diffusion limited. The inverse correlation between the fluid advection rate and the Cu^{2+} outflow concentration is the result of a higher dilution of fluid enriched in $Cu^{2+}_{(aq)}$ leaving the grain at a higher advection rate given a higher transport rate of $Cu^{2+}_{(aq)}$ depleted fluid transported around the grain. The increase in the $Cu^{2+}_{(aq.)}$ outflow concentration with an increase in the chalcopyrite to gangue mineral radius ratio is initially counter intuitive as one could think the relative decrease in chalcopyrite surface area leads to lower reaction rates. However, the surface area of the gangue mineral controls to diffusive flux of ions to the chalcopyrite surface area. A larger gangue mineral surface area captures more ions including protons and $Fe^{3+}_{(aq.)}$ required for the chalcopyrite dissolution from the ambient fluid into the grain. This result gives further evidence for the control of chalcopyrite dissolution rate by the diffusive flux through the gangue mineral.

4.4 Conditions and impact of coupled dissolution and reprecipitation (CDR)

Hypothetically, the rate of chalcopyrite dissolution and the potential of coupled chalcopyrite dissolution and reprecipitation of jarosite are controlled by three principal conditions:

Firstly, the composition of the inflow solution controls the availability of ions involved in the set of coupled reactions. For example, our results showed that low SO_4^{2-} inflow concentrations (10^{-13} M) inhibit jarosite precipitation, while high inflow SO_4^{2-} concentrations (10^{-5} M) resulted in jarosite supersaturation and precipitation at the chalcopyrite surface.

Secondly, the rates of the coupled reactions are important as certain aqueous species are concurrently consumed and produced. The coupling of species consumption and production can be summarized as follows: Fe^{2+} is produced by the proton-promoted (Eq. 6) and the ferric iron-promoted (Eq. 7) dissolution of chalcopyrite and can be consumed by the oxidation with O_2 (Eq. 9). Fe^{3+} is consumed by the ferric iron-promoted dissolution of chalcopyrite (Eq. 7) and jarosite precipitation (Eq. 4) and produced by the Fe^{2+} oxidation reaction (Eq. 9). SO_4^{2-} is consumed by the jarosite precipitation reaction (Eq. 8) and is produced by the ferric iron-promoted chalcopyrite dissolution reaction (Eq. 7) and H_2S oxidation reaction (Eq. 6). H^+ is consumed by the proton-promoted chalcopyrite dissolution mechanism (Eq. 2) and Fe^{2+} oxidation (Eq. 5) while it is produced by ferric iron-promoted chalcopyrite dissolution (Eq. 3) and sulphide oxidation (Eq. 10). The coupling of concurrent aqueous species production and consumption has been shown earlier to control the concentration of species and the development of a steady state balance between production and consumption rates (37). In our simulations we observed the concurrent production of Cu^{2+} and H^+, while Fe^{3+} was consumed at the chalcopyrite surface when jarosite precipitated (Fig. 5). This could, however, change for a range of reasons. For example, as jarosite precipitation reduces porosity, the diffusion of H^+ and Fe^{3+} to the chalcopyrite surface reduces. Similarly, if the pH is too high for significant H^+ - promoted chalcopyrite dissolution and respective H^+ consumption (Eq. 6), more net production of H^+ will occur due to the Fe^{3+} - promoted dissolution (Eq. 7) and jarosite precipitation (Eq. 8).

Thirdly, reaction rates can be controlled by the rate of ion transport to and away from the reaction site or by the inherent kinetic control of the reaction (38). In case of a reaction rate controlled by transport the reaction rate varies with the flow velocity or the diffusive flux while kinetically controlled reactions do not vary with the transport rate.

We investigated CDR processes at the surface of chalcopyrite through a series of reactive-transport simulations. In order to study conditions of coupled chalcopyrite dissolution and jarosite reprecipitation at the chalcopyrite mineral surface, the sulphate inflow concentration was varied between $5*10^{-5}$ and $9*10^{-5}$ mol/L while all other conditions remained the same (simulations 7 and 8, Fig. 6). The mineral saturation state for jarosite was initially highly undersaturated at the outflow in both cases (Fig. 6e). Three temporal phases reflecting different process can be observed: The initial increase in the $Cu^{2+}_{(aq.)}$ outflow concentration was the same as in a comparable simulation with very low sulphate concentration (simulation 4); porosity remained constant and jarosite precipitation did not occur. During this phase sulphide was mobilized and oxidized to sulphate according to the ferric iron-promoted chalcopyrite dissolution (Eq. 7) leading to a local enrichment in sulphate. The second phase commenced when the sulphate concentration in the jarosite precipitation zone was high enough to reach jarosite saturation (Fig. 4e). At this point jarosite started to precipitate and to accumulate and porosity started to decline in the jarosite precipitation zone. Consequently, ion transport to the chalcopyrite surface and the associated rate of chalcopyrite dissolution declined and the $Cu^{2+}_{(aq.)}$ outflow concentration decreased. The third phase was characterized by an exponential decline in a) the $Cu^{2+}_{(aq.)}$ outflow concentration, b) the porosity and c) the rate of jarosite accumulation in the jarosite precipitation domain. This phase resulted in the shutdown of $Cu^{2+}_{(aq.)}$ mobilization due to the coupled dissolution and reprecipitation at the chalcopyrite surface. The two simulations with an inflow composition undersaturated with respect to jarosite (simulations 7 and 8) illustrate the importance of the inflow composition. Given $Fe^{3+}_{(aq.)}$ contributes to chalcopyrite dissolution, one needs to keep the potassium and / or sulphate concentrations low to avoid jarosite precipitation. Previous experimental studies suggested using sulphuric acid with a sulphate concentration of $100 * 10^{-3}$ mol/L (31) or seawater with a sulphate concentration of $28 * 10^{-3}$ mol/L (39) as a lixiviant in areas with limited freshwater resources. However, such high sulphate concentrations would highly limit $Fe^{3+}_{(aq.)}$ concentrations and lead to abundant jarosite precipitation including precipitation at the surface of chalcopyrite where additional sulphate is formed. Given the critically important reaction of jarosite precipitation within a 10 µm zone at the chalcopyrite surface further suggests mesocosm experiments may show systemwide changes in the water composition but may not reveal clues on mineral surface reactions causing surface passivation and respective decline in the dissolution rate of a primary mineral.

This study has successfully developed a reactive-transport model integrating reactions at a discrete mineral surface with continuum-scale domains enabling the prediction of coupled dissolution and replacement reactions (CDR) at a mineral surface. Specifically, jarosite precipitation at the chalcopyrite surface was predicted at given conditions. However, the formation of another secondary mineral in the form of covellite (40) and the potential transformation of jarosite to iron oxides (41) have been demonstrated under certain conditions, which have not been explored here. As pointed out earlier (9), variations in chemical and physical conditions from the micro- to macro-scale can lead to different CDRs at the mineral surface and warrant further investigations. Specifically, electrochemical conditions can impose redox-controlled mineral dissolution and surface passivation of metal sulphide minerals such as pyrite and chalcopyrite (42 and references herein), which has not been addressed in this study.

5 Conclusions

A reactive-transport model has been developed to predict coupled dissolution and reprecipitation reactions (CDR) at mineral surfaces and was applied to reveal reactions at the chalcopyrite mineral surface and the consequences for copper recovery in heap leaching systems. Proton-promoted chalcopyrite dissolution exceeded ferric iron-promoted dissolution of chalcopyrite under the given conditions. Reactions at the mineral surface were transport-limited where the diffusive flux of ions through the gangue mineral (quartz) surrounding chalcopyrite controlled the reaction rates. Ferrous iron oxidation is negligible under the very low pH conditions, whereas sulphide oxidation did occur near the chalcopyrite surface leading to elevated sulphate concentrations. Once the solution at the mineral surface reached thermodynamic equilibrium with jarosite, jarosite precipitation commenced leading to a reduction in porosity within the precipitation zone. As a consequence, ionic transport became increasingly restricted and ultimately terminated chalcopyrite dissolution and copper mobilization. It is recommended to keep sulphate concentrations low in the infiltrating solution to avoid jarosite precipitation. The study illustrates how processes at micro-meter scale can control systemwide changes in fluid composition, in this case copper recovery in low-grade ore heap leaching systems.

Acknowledgement

The authors wish to acknowledge earlier discussions with Dr. Eric Ansah and Dr Jay Black from The University of Melbourne on copper dissolution in heap systems. The authors further wish to thank the three reviewers for their constructive comments.

References

1. Elshkaki, A, Graedel, T.Ez., Ciacci, L., & Reck, B.K. (2016). Copper demand, supply and associated energy use to 2050. *Global Environmental Change* 39, 305-315. https://doi.org/10.1016/j.gloenvcha.2016.06.006

2. Mudd, G.M., Weng, Z., & Jowitt, S.M. (2013). A detailed assessment of the global Cu resource trends and endowments. *Economic Geology* 108 (5), 1163-1183. https://doi.org/10.2113/econgeo.108.5.1163

3. Kelly, T.D., & Matos, G.R., (2014). Historical statistics for mineral and material commodities in the United States (2014), US Geological Survey Data Series 140. https://www.usgs.gov/centers/national-minerals-information-center/historical-statistics-mineral-and-material-commodities (Accessed July 2025)

4. Schipper, B.W., Lin, H.-C., Meloni, M.A., Wansleeben, K., & Heijungs R. (2018). Estimating global copper demand until 2100 with regression and stock dynamics. *Resources, Conservation and Recycling* 132, 28-36. https://doi.org/10.1016/j.resconrec.2018.01.004

5. Hackl, R.P., Dreisinger, D.B., Peters, E., & King, J.A. (1995). Passivation of chalcopyrite during oxidative leaching in sulfate media. *Hydrometallurgy* 39 (1-3), 25-48. https://doi.org/10.1016/0304-386X(95)00023-A

6. Putnis, A. (2002). Mineral replacement reactions: from macroscopic observations to microscopic mechanisms. *Mineralogical Magazine* 66 (5), 689-708, https://doi.org/10.1180/0026461026650056

7. Putnis A. (2009). Mineral replacement reactions. In: Oelkers E.H., Schott E.H. (Eds.), Thermodynamics and kinetics of water-rock interactions. *Reviews in Mineralogy and Geochemistry* (2009) 30, 87-124, https://doi.org/10.2138/rmg.2009.70.3

8. Ruiz-Agudo, E., Putnis, C.V., & Putnis, A. (2014). Coupled dissolution and precipitation at mineral-fluid interfaces. *Chemical Geology* 383, 132-146, https://doi.org/10.1016/j.chemgeo.2014.06.007

9. Altree-Williams, A., Pring, A., Ngothai, Y., & Brugger, J. (2015). Textural and compositional complexities resulting from coupled dissolution-reprecipitation reactions in geomaterials. *Earth-Science Reviews* 150, 628-651, https://doi.org/10.1016/j.earscirev.2015.08.013

10. Harlov, D.E., Wirth, R., & Hetherington, C.J. (2011). Fluid-mediated partial alteration in monazite: the role of coupled dissolution-reprecipitation in element mobilization and mass transfer. *Contributions to Mineralogy and Petrology* 162, 329-348, https://doi.org/10.1007/s00410-010-0599-7

11. Manecki, M., Kwaśniak-Kominek, M., Majka, J.M., & Rakovan, J. (2020). Model of interface-coupled dissolution-precipitation of pseudomorphic replacement reaction in aqueous solutions based on the system of cerussite $PbCO_3$-pyromorphite Pb5(PO4)3Cl. *Geochimica Cosmochimica Acta* 289, 1-13, https://doi.org/10.1016/j.gca.2020.08.015.

12. Deng, H., Poonoosamy, J. & Molins, S. (2022) A reactive transport modelling perspective on the dynamics of interface-coupled dissolution-precipitation. *Applied Geochemistry* 137, https://doi.org/10.1016/j.apgeochem.2022.105207

13. Emmanuel S. (2022) Modeling the effect of mineral armoring on the rates of coupled dissolution-precipitation reactions: Implications for chemical weathering. *Chemical Geology* 601, https://doi.org/10.1016/j.chemgeo.2022.120868

14. Wang, Z., Hu, M. & Steefel, C. (2024) Pore-scale modeling of reactive transport with coupled mineral dissolution and precipitation. *Water Resources Research* 60, https://doi.org/10.1029/2023WR036122

15. Bouffard, S.C. & Dixon, D.G. (2001). Investigative study into the hydrodynamics of heap leaching processes. *Metallurgical and Material Transactions B* 32, 763-776, https://doi.org/10.1007/s11663-001-0063-1

16. Cariaga, E., Concha, F., & Sepúlveda, M. (2005). Flow through porous media with applications to heap leaching of copper ores. *Chemical Engineering Journal* 111(2-3), 151-165, https://doi.org/10.1016/j.cej.2005.02.019

17. Mostaghimi, P., Tollit, B.S., Neethling, S.J., Gorman, G.J., & Pain, C.C. (2014). A control volume finite element method for adaptive mesh simulation of flow in heap leaching. *Journal of Engineering Mathematics* 87, 111-121, http://dx.doi.org/10.1007/s10665-013-9672-3

18. McBride. D., Cross, M., & Gebhardt, J.E. (2012). Heap leach modeling employing CFD technology: a 'process' heap model. *Minerals Engineering 33*, 72-79, https://doi.org/10.1016/j.mineng.2011.10.003

19. McBride, D., Croft, T.N., Cross, M., Bennett, C., & Gebhardt, J.E. (2014). Optimization of a CFD–Heap leach model and sensitivity analysis of process operation. *Minerals Engineering* 63, 57-64, https://doi.org/10.1016/j.mineng.2013.11.010

20. Dixon, D.G. &, Hendrix, J.L. (1993). A mathematical model for heap leaching of one or more solid reactants from porous ore pellets. *Metallurgical Transactions B* 24: 1087-1102, https://doi.org/10.1007/BF02661000

21. Kimball, B.E., Rimstidt J.D., & Brantley, S.L. (2010). Chalcopyrite dissolution rate laws. *Applied Geochemistry 25* (7), 972-983, https://doi.org/10.1016/j.apgeochem.2010.03.010

22. Li, Y., Kawashima, N., Li, J, Chandra, A.P., & Gerson, A.R. (2013). A review of the structure, and fundamental mechanisms and kinetics of the leaching of chalcopyrite. *Advances in Colloid Interface Science* 197, 1-32, https://doi.org/10.1016/j.cis.2013.03.004

23. McBride, D., Gebhardt, J., Croft, N., Cross, M., (2018). Heap Leaching: Modelling and forecasting using CFD technology. *Minerals 8*(1), 9, https://doi.org/10.3390/min8010009

24. Leahy, M.J., & Schwarz, M.P. (2009). Modelling jarosite precipitation in isothermal chalcopyrite bioleaching columns. *Hydrometallurgy 98* (1-2), 181-191, https://doi.org/10.1016/j.hydromet.2009.04.017

25. Nardi, A., Idiart, A., Trinchero, P., de Vries, L.M., & Molinero, J. (2014) Interface COMSOL-PHREEQC (iCP), an efficient numerical framework for the solution of coupled multiphysics and geochemistry. *Computer and Geosciences* 69*,* 10-21, https://doi.org/10.1016/j.cageo.2014.04.011

26. Silva, O., Nardi, A., Román-Ross, G., Molinero, J., & Quesada, P. (2014). Hydro-Mechanical-Chemical Coupled Modeling of Copper Heap Leaching with iCP. Iberian COMSOL Multiphysics Conf (2014) 26-28, https://www.comsol.com/paper/download/210581/IberianCOMSOLConference.pdf.

27. Jyoti, A., & Haese, R.R. (2021) Validation of a multicomponent reactive-transport model at pore scale based on the coupling of COMSOL and PhreeqC. *Computers and Geoscience* 156, doi.org/10.1016/j.cageo.2021.104870.

28. Mollins, S., Soulaine, C., Prasianakis, N., Abbasi, A., Poncet P. & others (2021) Simulation of mineral dissolution at the pore scale with evolving fluid-solid interfaces: Review of approaches and benchmark problem set. *Computational Geosciences* 25, 1285-1318, https://doi.org/10.1007/s10596-019-09903-x

29. Soulaine, C. (2024) Micro-continuum modeling: A hybrid-scale approach for solving coupled processes in porous media. *Water Resources Research* 60, https://doi.org/10.1007/s10596-019-09903-x

30. Bear, J., (1972). *Dynamics of fluids in porous materials.* Society of Petroleum Engineers, 764 pp.

31. Schulz, H.D., (2000). Quantification of early diagenesis: Dissolved constituents in pore water and signals in solid phase. In: Zabel M, Schulz HD, editors. Marine Geochemistry. Berlin, Heidelberg, New York: Springer, p. 73-124.

32. Marty, N.C., Claret, F., Lassin, A., Tremosa, J., Blanc, P., et al. (2015). A database of dissolution and precipitation rates for clay-rocks minerals. *Applied Geochemistry 55,* 108-118, https://doi.org/10.1016/j.apgeochem.2014.10.012

33. Singer, P.C., & Stumm, W. (1970). The solubility of ferrous iron in carbonate-bearing waters. *Journal of the American Water Work Association* 62 (3), 198-202, https://doi.org/10.1002/j.1551-8833.1970.tb03888.x

34. Bouffard, S.C. & West-Sells, P.G. (2009) Hydrodynamic behavior of heap leach piles: Influence of testing scales and material properties. *Hydrometallurgy* 98, 136-142, https://doi.org/10.1016/j.hydromet.2009.04.012

35. Robertson, S. (2017) Development of an integrated heap leach solution flow and mineral leaching model. *Hydrometallurgy* 169, 79-88, https://doi.org/10.1016/j.hydromet.2016.12.010

36. Ansah, E.O., Black, J. & Haese, R.R. (2025) Impact of mineral dissolution – precipitation on pore geometry during copper sulphide heap leaching. *Minerals Engineering* 230, https://doi.org/10.1016/j.mineng.2025.109379

37. Phukan, M., Vu, H.P., & Haese, R.R. (2021). Mineral dissolution and precipitation reactions and their net balance controlled by mineral surface area: an experimental study on the interactions between continental flood basalts and CO2-saturated water at 80 bars and 60° C. *Chemical Geology 559*, https://doi.org/10.1016/j.chemgeo.2020.119909

38. Brantley, S., (2008). Kinetics of Mineral Dissolution, In: Brantley, S., Kubicki, J., White, A., Editors. Kinetics of Water-Rock Interaction. New York (NY): Springer, 151-210. https://doi.org/10.1007/978-0-387-73563-4_5

39. Hiroyoshi, N., Hirota, M., Hirajima, T., & Tsunekawa, M., (1997). A case of ferrous sulfate addition enhancing chalcopyrite leaching. *Hydrometallurgy* 47, 37-45.

40. Velásquez-Yévenes, L., & Quezada-Reyes, V., (2018). Influence of seawater and discard brine on the dissolution of copper ore and copper concentrate. *Hydrometallurgy* 180, 88-95, https://doi.org/10.1016/j.hydromet.2018.07.009Get rights and content

41. Ren, Z., Chao, C., Krishnamoorthy, P., Asselin, E., Dixon, D.G., et al. (2022). The overlooked mechanism of chalcopyrite passivation. *Acta Materialia* 236, https://doi.org/10.1016/j.actamat.2022.118111

42. Elwood Madden, M.E., Madden, A.S., Rimstidt, J.D., Zahrai, S., Kendall, M.R., et al. (2012). Jarosite dissolution rates and nanoscale mineralogy. *Geochimica Cosmochimica Acta* 91: 306-321, https://doi.org/10.1016/j.gca.2012.05.001

43. Teimouri, S., Potgieter, J. H. & Billing, C. (2025) A comparison of the electrochemical oxidative dissolution of pyrite and chalcopyrite in dilute nitric acid solution. *ChemistryOpen* 14, https://doi.org/10.1002/open.202400053

Supplementary Information (SI)

1. Details of Fluid Flow and Transport modelling:

The Navier-Stokes equation (SI Eq. 1) and mass conservation equation (SI Eq. 2) are used to define the local velocity distribution

$$\rho\frac{\partial \boldsymbol{u}}{\partial t} = \mu\nabla^2\boldsymbol{u} - \rho(\boldsymbol{u}.\nabla)\boldsymbol{u} - \nabla p\Big|_{\Gamma_{\text{pores}}} \qquad \text{SI (1)}$$

$$\nabla.(\rho\boldsymbol{u}) = 0|_{\Gamma_{\text{pores}}} \qquad \text{SI (2)}$$

Here $\boldsymbol{u}$ (m s^{-1}) is the velocity of the fluid, μ ($\text{kg m}^{-1}\text{ s}^{-1}$) is the fluid viscosity, ρ (kg m^{-3}) is the fluid density and p (Pa) is the pressure field.

Together with the above-mentioned equations, the Brinkman equation is solved which is a combination of the continuity equation and the momentum equation and is defined for an incompressible flow according to (14):

$$\text{SI (3)}$$

$$\frac{\rho}{\emptyset}\left(\frac{d\boldsymbol{u}}{dt} + (\boldsymbol{u}\cdot\nabla)\frac{\boldsymbol{u}}{\emptyset}\right) = \nabla\cdot\left[-p + \frac{\mu}{\emptyset}\big(\nabla\boldsymbol{u} + (\nabla\boldsymbol{u})\big) - \frac{2}{3}\mu(\nabla\cdot\boldsymbol{u})\right] - \left(\mu K^{-1} + \frac{Q}{\emptyset^2}\right)\boldsymbol{u}\Big|_{\Gamma_{\text{qaurtz + jarosite}}}$$

$$\nabla.(\rho\boldsymbol{u}) = \text{Q}|_{\Gamma_{\text{qaurtz + jarosite}}} \qquad \text{SI (4)}$$

Here $\emptyset$ is the porosity and K (m^2) is the permeability of the porous media and Q is a mass source/sink term.

2. Details of the advection-diffusion-reaction equation:

The standard reactive-transport equation is used combining terms for advection, diffusion and reaction:

$$\frac{\partial c_i}{\partial t} = \underbrace{-\nabla\cdot(\boldsymbol{u}c_i)}_{Advection} + \underbrace{\nabla\cdot\big(\nabla D_{Diff}c_i\big)}_{Diffusion} + \underbrace{R_i}_{Reaction}\Bigg|_{\Gamma_{\text{qaurtz + jarosite + pores}}} \qquad \text{SI (5)}$$

Here, $\boldsymbol{u}$ (m s^{-1}) is the fluid velocity, c_i (mol m^{-3}) is the concentration of species i transported through the pore scape and porous media domains ($\Gamma_{\text{qaurtz + jarosite + pores}}$), D_{diff} ($\text{m}^2\text{ s}^{-1}$) is the diffusion coefficient and R_i ($\text{mol m}^{-3}\text{ s}^{-1}$) is the rate of a chemical reaction contributing to the concentration of the species i through homogeneous reaction like aqueous speciation and kinetic reactions taking place in the bulk fluid. Advection and diffusion are accounted for by the first and the second term on the right-hand side of the equation. A multi-component reactive transport formulation where the transport equation is solved for each element in the chemical system is used. Reactions occurring at the boundary are not included in this equation, explicit definition of these reactions are defined in the following section.

The initial conditions in the model were defined as follows:

$$\begin{bmatrix} \boldsymbol{u}_x = 0 \\ \boldsymbol{u}_y = 0 \\ p \ \ = 0 \end{bmatrix} \qquad \text{SI (6)}$$

3. Rate equations for reactions used in the study:

The rate of chalcopyrite dissolution according to the ferric iron dissolution mechanism is defined as

$$\acute{R}_{Fe} = 10^{1.88}\mathrm{e}^{-48100/RT}[\mathrm{H}^{+}]^{0.8}(\mathrm{Fe(III)})^{0.42}\Big|_{\gamma_{\mathrm{chalcopyrite}}} \qquad \text{SI (7)}$$

The rate of chalcopyrite dissolution according to the proton-promoted dissolution mechanism is defined as

$$\acute{R}_{H} = 10^{-1.52}\mathrm{e}^{-28200/RT}[\mathrm{H}^{+}]^{1.68}\Big|_{\gamma_{\mathrm{chalcopyrite}}} \qquad \text{SI (8)}$$

Here, $\acute{R}_{Fe}$ and $\acute{R}_{H}$ are the reaction rates for Eq. 8 and 9 in the manuscript, respectively. $[\mathrm{H}^{+}]$ and $(\mathrm{Fe(III)})$ are the activity of protons and ferric ions, respectively, R is the ideal gas constant (8.314 J mol^{-1} K^{-1}) and T (K) is the temperature.

The kinetically controlled dissolution of quartz can be defined as:

$$SiO_2 + 2H_2O = H_4SiO_4 \qquad \text{SI (9)}$$

And the reaction rate can be defined as:

$$R_{quartz} = SA_{quartz}\left[A_i^{298}e^{-\frac{E_a}{R}}\prod(a_{ij}^{n})(1-\Omega_{quartz}^{p_i})^{q_i}\right]\Bigg|_{\Gamma_{\mathrm{qaurtz}}} \qquad \text{SI (10)}$$

R_{quartz} is the reaction rate in mol s^{-1}. SA_{quartz} is the surface area of the quartz mineral, which is calculated as 22.64 m^2 kgw^{-1} assuming the quartz grain is a sphere with a diameter of 0.0001 m, it has a smooth surface and a density of 22.65 Kg m^{-3}. Given the short simulation times and the slow dissolution rate of quartz, the geometry of the quartz grain did not evolve with time. The Arrhenius pre-exponential factor A_i^{298} (mol $\mathrm{m}^2\mathrm{s}^{-1}$), is calculated from k_i the log rate constant ($\log \mathrm{mol}\ \mathrm{m}^2\mathrm{s}^{-1}$) and Arrhenius activation energy E_a (kJ mol^{-1}) at 25 °C and a pH=0. T is the temperature in K and R is the ideal gas constant (8.314 J mol^{-1} K^{-1}). Here Ω is the saturation state of the quartz, n represents the reaction order with respect to the species H^{+}. The chemical affinity parameters p_i and q_i in most cases is unity unless specified. The parameters used for the kinetic dissolution at different reaction conditions are listed in SI Table 1 below.

SI Table 1: Parameters used for the reaction rate of quartz (adopted from [27]).

	Acid	Neutral	Base
A_i^{298} (mol $\mathrm{m}^2\mathrm{s}^{-1}$)	0	1.98	1.97E+04
E_a (kJ mol^{-1})	0	77	80
n	0	0	0.34

The rate equation for the oxidation of ferrous iron is given as:

$$R_{Fe^{2+}} = -\left(2.91e^{-9} + 1.33e^{12}\,\alpha_{OH^-}^2\,P_{O_2}\right)m_{Fe^{2+}}\Big|_{\Gamma_{\text{qaurtz+pores+jarosite}}} \qquad \text{SI (11)}$$

Here $\alpha_{OH^-}^2$ is the activity of the hydroxyl ion, $m_{Fe^{2+}}$ is the total molality of ferrous iron in solution, and P_{O_2} is the oxygen partial pressure (atm).

SI Table 2: Aqueous speciation reactions used in the model (adopted from the phreeqc.dat database)

Reaction	$log\ K_{eq}$
$Fe^{2+} + H_2O = FeOH^-$	-9.5
$Fe^{2+} + 3H_2O = Fe(OH)_3^-$	-31.0
$Fe^{3+} + H_2O = Fe(OH)^{2+}$	-2.19
$Fe^{3+} + 2H_2O = Fe(OH)_2^+$	-5.67
$Fe^{3+} + 3H_2O = Fe(OH)_3$	-12.56
$SO_4^{2-} + H^+ = HS^- + 2O_2$	-125.0